Article

Inverse Thermal Analysis as a Tool for Optimizing Concentrated Solar Energy Elaboration of Wear Resistant Surface Layers

Anna D. Zervaki [1], Samuel G. Lambrakos [2], Athanasios G. Mourlas [3], Ioannis G. Papantoniou [4,5], José Rodríguez [6] and Pandora P. Psyllaki [3,*]

1 Shipbuilding Technology Laboratory, School of Naval Architecture and Marine Engineering, National Technical University of Athens, 9 Heroon Polytechniou Ave., 157 73 Athens, Greece
2 U.S. Naval Research Laboratory, Washington, DC 20375, USA
3 Surface Engineering Laboratory, Department of Mechanical Engineering, University of West Attica, 250 Thivon & P. Ralli Str., Ancient Olive Grove Campus, 122 41 Egaleo, Greece
4 Laboratory of Manufacturing Technology, School of Mechanical Engineering, National Technical University of Athens, Heroon Polytechniou 9, 157 80 Athens, Greece
5 Department of Naval Architecture, School of Engineering, University of West Attica, Ag. Spyridonos Str., Egaleo Park Campus, 122 43 Egaleo, Greece
6 CIEMAT-Plataforma Solar de Almería, Aptdo, 22, 04200 Tabernas, Spain
* Correspondence: psyllaki@uniwa.gr; Tel.: +30-210-5381292

Abstract: Concentrated Solar Energy (CSE) processing is considered a promising renewable energy source technique for elaborating thick, wear-resistant claddings onto metallic surfaces of large dimensions that are expected to operate in heavy duty applications, such as excavator shovels, mineral crushers, etc. However, the prediction of surface processing effects on the microstructure and the properties of the main construction base metal are of crucial importance, as they are commonly required in all surface modification techniques. Thus, the present study is focused on the inverse thermal analysis and parametric modeling of heat deposition associated with CSE surface processing of metals. In this preliminary attempt, experimental findings that concern the elaboration of TiC- and chromium carbide-reinforced clads onto common steel base metals were used to quantify the evaluation of the temperature histories within the volume of workpieces undergoing solar heating, where direct temperature measurements contain uncertainties and/or are not even possible. Results of prototype inverse thermal analyses of heat transfer in processed layer-substrate systems are presented, demonstrating the general aspects of a parametric model for thermal analysis and simulation.

Keywords: inverse thermal analysis; parametric modeling; concentrated solar energy processing; cladding; wear-resistant surface layers

1. Introduction

Concentrated Solar Energy (CSE), that is, the production of medium- to high-temperature heat by means of movable mirrors that track the sun and concentrate its radiation on a focal point/area has been proposed, among others, as a "green" technique for implementing surface modifications of metallic substrates [1], leading to surface layers of superior performance during operation via surface hardening [2,3], gas nitrating [4], cladding [5–8] and surface alloying [7,9]. Almost twenty-five years ago, Flamant et al. [3] introduced solar processing to perform such high temperature material treatments, documenting on technical and economic data, when comparing concentrated solar beams to other nonconventional ones, namely laser and plasma. Although the capital cost of such solar systems is higher than those of laser and plasma sources, the higher overall energy efficiency and the feasibility of treating surfaces of much larger dimensions are attractive, important features for considering concentrated solar energy for applications in the specific field of surface modification of solids. Despite its

main disadvantage related to the sun availability [10], CSE remains a promising alternative to conventional heat sources [11] for specific applications, such as cladding of large dimension metallic surfaces.

The feasibility of CSE treatment in the field of materials science and metallurgy has been proven for various processes and several materials. However, the heat effects during the whole processing history of the treated material are still a matter of concern for the relevant scientific community, since the metallurgical transformations take place not only during solar exposure, but they last during cooling from above or near melting to ambient temperature, controlling in this way the microstructure and the properties of both the directly solar-treated layer, as well as those of the underlying material.

In the case of solar cladding process of AISI 316 stainless steel over AISI 1026 common steel [12], the satisfactory agreement between experimental observations and numerical simulation results carved out a solid base for further optimization of the solar cladding parameters. More precisely, stainless steel powder was pre-deposited on the base metal surface and the system was solar irradiated, whilst the temperature evolution of the base metal was recorded in real-time by the aid of K-type thermocouples welded at three different locations on the opposite side of the irradiated surface. These results, together with the thermophysical properties of the material system, were used to develop and validate a finite element model (FEM) that could reliably predict the level and extent of the thermal fields that occurred during solar processing. Microscopic observations revealed, mainly, the dendritic structure of the obtained clads and verified further the good agreement to the numerical thermal model's predictions.

In order to improve the homogeneity inside the test chamber for materials processing [13], a numerical thermal model was developed, taking as main assumptions that heat transfer occurs via: (i) conduction through the receiver plate; (ii) radiation between the up-plate and the down-plate; (iii) natural convection between the plates and the surrounding medium. For the validation of the numerical model, two materials of vastly different physical properties -thermal conductivity, specific heat capacity and emissivity- were used as receivers (up-plates) under three set-up configurations and the temperature evolution was recorded in real-time by the aid of a set of five K-type thermocouples placed at specific locations of the tested materials system. The combined evaluation of the numerical simulation and experimental results revealed that the thermal fields developed during solar irradiation are controlled by the thermal properties of both the down–plate and the surrounding medium; thus, the optimization of a required solar processing is strongly dependent on the proper selection of the set-up configuration and not exclusively on the solar irradiation parameters.

In the case where solar processing incorporates melting of the irradiated materials, as in welding [14], the thermal fields developed under the constraints imposed by the particular experimental configuration and solar exposure parameters determine also the microstructure obtained during materials re-solidification, as well as that of the heat affected zone (H.A.Z.). In the case of solar sintering of Al_2O_3-based ceramics [15], high levels of densification of the green bodies were achieved, which cannot be obtained by conventional sintering in electric furnaces without applying pressure. The relevant dense microstructure obtained was attributed to the high heating rates and short sintering duration during solar treatment that restrained grain growth, whilst the use of a $95N_2$:$5H_2$ mixture as surrounding medium was found to result in pores elimination. Similar observations were reported in the case of solar sintering of Ni-Zn ferrites [16]; compared to sintering in conventional electric furnace, the solar-based technique led to ferrites of higher densification that influenced both their mechanical and magnetic properties.

Solar sintering of bulk carbide-reinforced metallic-matrix composites [17] was achieved by pre-mixing vanadium carbide and AISI M2 high speed steel powders, and successive solar exposure using (a) Fresnel lens and (b) solar furnace, for various reinforcing particles percentages and treatment parameters. The experimental results revealed the high

microstructural quality of the treated material and are significantly encouraging for performing further such metallurgical processes via concentrated solar energy.

Finally, the particular thermal cycles during solar processing, that is, high heating rate and controlled dwell time at a temperature level, as well as the thermal field implied in the receiver's volume allowed foaming of Al-Si precursors and led to stable porous metallic structures, overcoming the common drawback of pore collapse when thermal treatment takes place in electric furnaces [18].

Inverse analysis of volumetric heat-deposition processes [19–24], for example, welding [25,26], poses a specific problem, which follows from the unique characteristics and relative complexity of such processes. These processes are typically characterized by regions of volumetric heat deposition having complex shapes and heat-source-workpiece interactions. Modeling and inverse analysis of thermal processes within these regions of volumetric deposition, for example, inverse thermal analysis, remains an open problem, distinct from other problems of inverse analysis. Heat-deposition fields, for example, temperature fields, associated with these processes are a function of the nature of the energy source interaction (or coupling) with the ambient medium. The general characteristics of interactions between sources and ambient media, especially for the case of energy-deposition processes such as welding, motivates a relatively well-defined posing of the problem for inverse analysis of deposition processes. This posing establishes the need for parametric models of deposition processes whose formulations are optimal for inverse analysis of complex source-ambient-medium interactions. For example, inverse thermal analysis of welding processes still remains an open problem, because of the complexity of energy-source-workpiece coupling related to the wide range of different welding processes [27].

The present study continues upon experimental research previously published by members of the authors' team [7,8], where the feasibility of using CSE technology for the elaboration of wear-resistant surface layers has been proven. Nevertheless, the evaluation of the temperature field within the workpiece is the crucial factor that controls the microstructure obtained in both the solar-treated surface layers and the underlying metal and, thus, their mechanical properties that finally affect the machinability of the so-treated workpiece using conventional tools, as well as the in-service performance of the surface-treated mechanical components. For this purpose, the particular work—part of which has been presented at the Advances in Welding & Additive Manufacturing Research Conference [28]—is targeted to the inverse thermal analysis and parametric modeling of heat deposition associated with the specific heat-deposition taking place during CSE surface processing, in order to describe temperature histories within the volume of the solar-treated workpieces, where direct temperature measurements contain uncertainties and/or are not even possible.

2. Materials and Methods

The inverse thermal analysis developed is based on microscopic observations of two CSE-treated materials systems, namely TiC and Cr_3C_2 powders pre-deposited onto similar carbon steel substrates, at the installations of Plataforma Solar de Almería, PSA (Spain), in particular at the horizontal solar furnace SF40 [29]. As mentioned above [7,8], the general aspects of the surface solar processing have been described in detail in previous works. Carbon steel (DIN 17100 St 37-2) specimens with dimensions $50 \times 70 \times 15$ mm were used as base metals on the polished surface on which the carbide powders were deposited, under preparation conditions such that no interactions between the powder and the substrate material could take place. More precisely, 3.37 g of TiC powder with a particle size distribution $-149 + 74$ μm and 5.71 g Cr_3C_2 powder with a particle size distribution of $-106 + 45$ μm had been manually deposited in the form of disks (⌀35, thickness: 1.5 mm), prior to solar processing (Figure 1a). The so-prepared specimens were placed at the center of the processing chamber (Figure 1b), onto a thermal insulating Al_2O_3 support and exposed to concentrated solar energy (Figure 1c) under continuous flow of Ar inert gas.
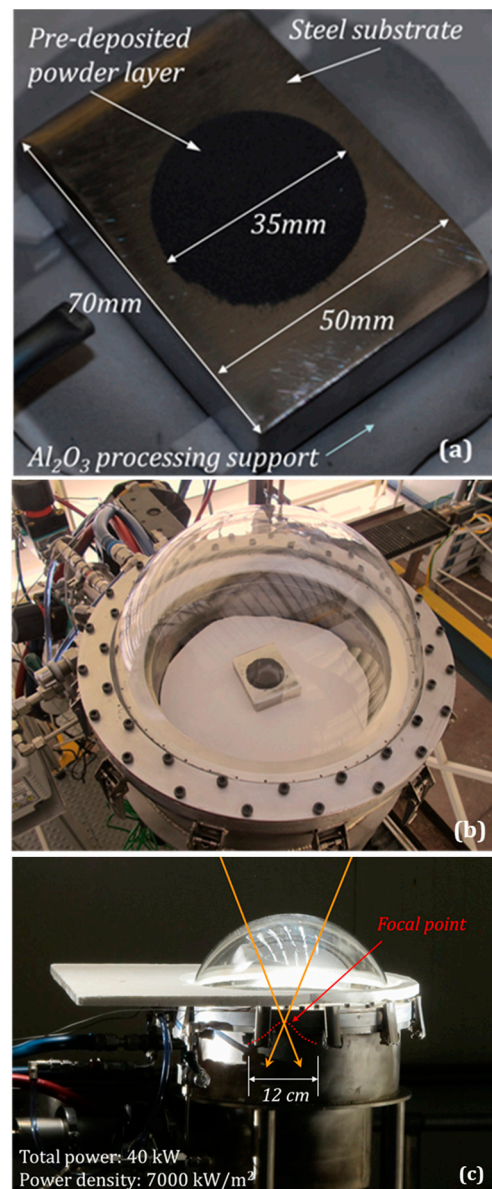
Figure 1. Experimental details for the CSE processing aiming to surface cladding: (**a**) material system to be solar-treated; (**b**) positioning of the prepared specimen in the processing chamber; (**c**) experimental arrangement for solar processing.

For both material systems, the microscopic observations provide quantitative results on both the extent and geometry of the surface layer that has been led to melting, and the underlying Heat Affected Zone (H.A.Z.), as well as on the metallurgical reactions taking place in the melt and its microstructure obtained during solidification.

3. Experimental Findings and Physical Model

The two material systems considered for prototyping solar-heating analysis in this study exhibited extremely different behavior [7]. In the case of TiC powder (Figure 2), the ceramic particles were dispersed in the liquid metallic matrix, without any metallurgical reaction with it, leading to a "clear" surface composite layer after cooling to ambient temperature (Figure 3). On the contrary, after sufficient solar exposure (Figure 4) the Cr_3C_2 particles were totally incorporated in the molten pool and diluted in it, leading to a new surface alloy rich in Cr rather than to a surface composite layer (Figure 5).
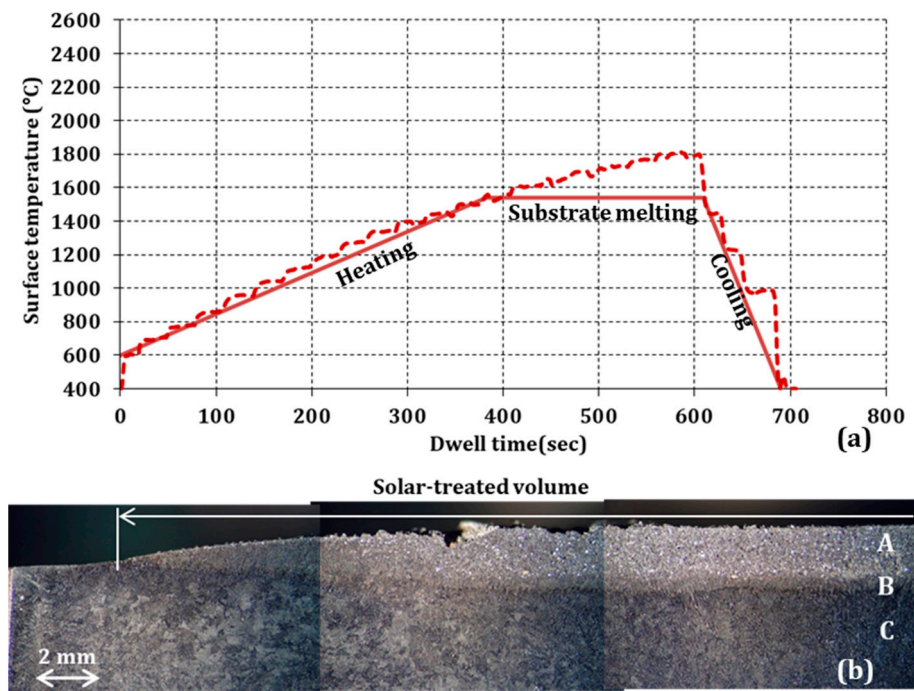
Figure 2. Solar processing of TiC/carbon steel system: (**a**) successive stages during solar processing (dashed line: experimental measurements, reproduced from [7], license number: 5545980711788); (**b**) half area of the solar-treated specimen obtained (stereoscope cross-section).
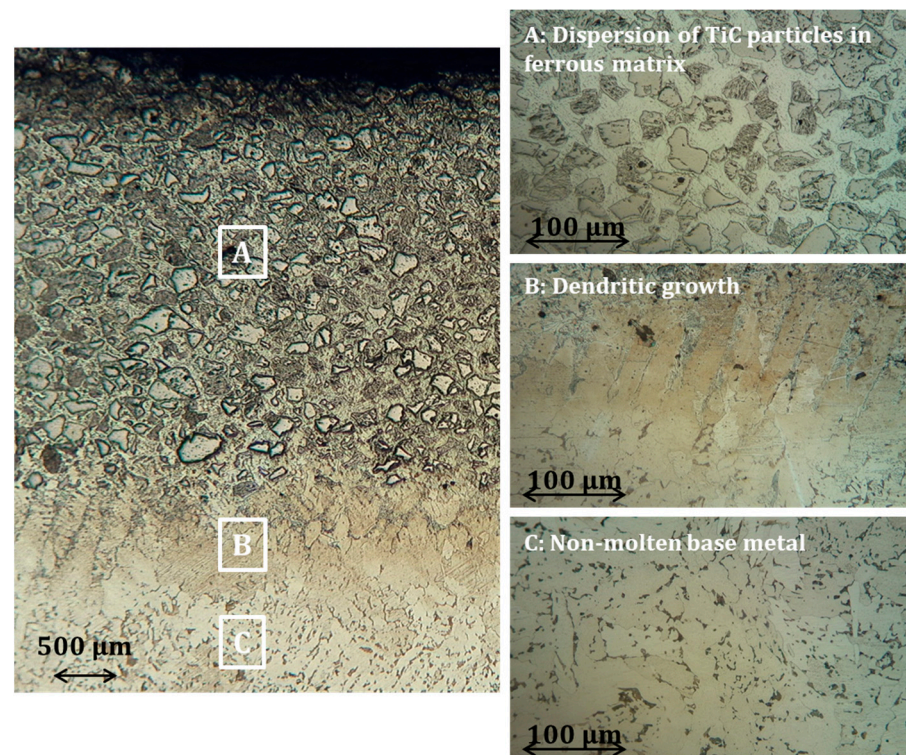

Figure 3. Optical micrograph of the solar-treated TiC/carbon steel system cross-section, where areas of different microstructure can be clearly identified (middle of the CSE-affected area). Areas marked as A, B and C on the left image, are presented in higher magnification at the right column.
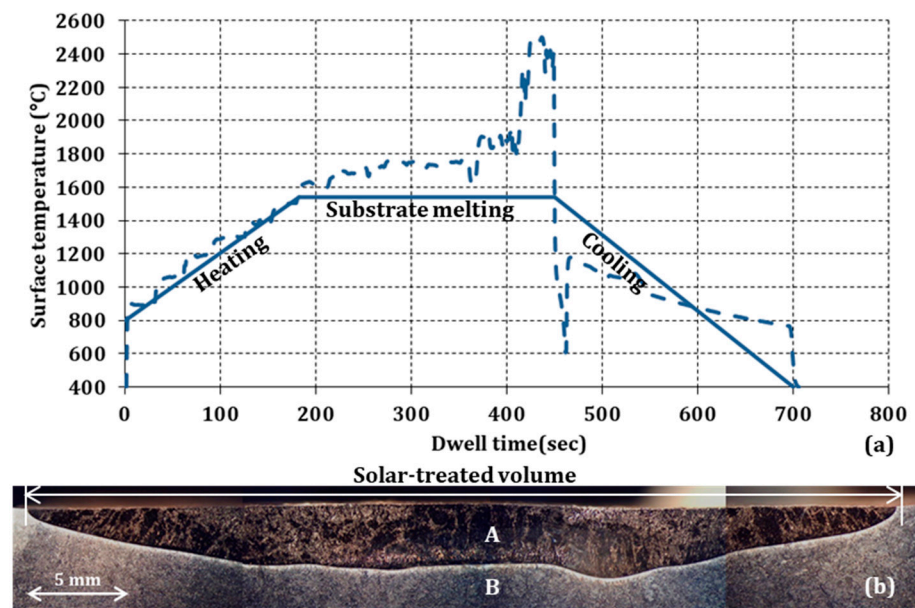
Figure 4. Solar processing of Cr_3C_2/carbon steel system: (**a**) successive stages during solar processing (dashed line: experimental measurements, reproduced from [7], license number: 5545980711788); (**b**) overall cross section of the solar-treated specimen obtained (stereoscope cross-section).
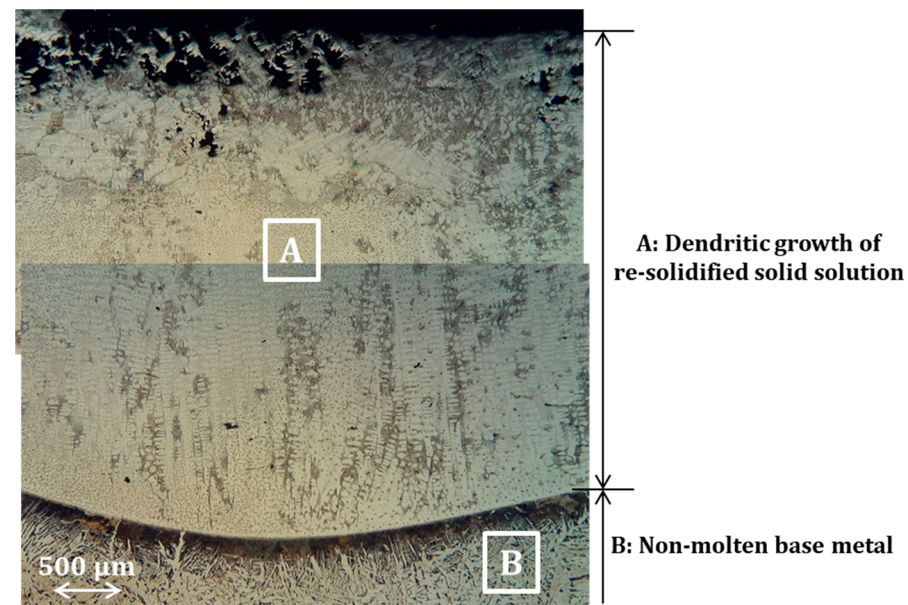

Figure 5. Optical micrograph of the solar-treated Cr_3C_2/carbon steel system cross-section, where areas of different microstructure can be identified (middle of the CSE-affected area).

During solar treatment, the surface temperatures of irradiated specimens were monitored in real-time via an optical pyrometer. It should be noted that with respect to inverse thermal analysis, it is assumed that the measured temperatures are estimates, owing to uncertainties due to liquid-surface movement during process-evolution and ambient vapor in the sealed testing bell-jar chamber.

Based on the above experimental findings, a generic physical model describing phenomena that take place during successive stages can be proposed (Figure 6):

- During heating at surface temperature below the melting temperature of the substrate (T_{max}: 1540 °C), the concentrated solar energy is absorbed only by the area covered by

the black-colored ceramic particles, while it is reflected by the noncovered polished surface of the base metal (Figure 6a).

- During heating at surface temperature above the melting temperature of the substrate, the solar energy absorbed results in progressive melting of the underlying metal and immersion of the pre-deposited powder in the melting pool (Figure 6b).

- Lasting the solar exposure of the workpiece, the depth of the melting pool increases and the circulation currents in the ferrous melt lead to the homogeneous distribution of the carbide particles in the liquid metal (Figure 6c). Depending on the nature of the incorporated carbides, they either remain non-attacked (TiC case), or are diluted in the molten steel (Cr_3C_2 case).

- During cooling to ambient temperature, the solidification of the melts follows the thermodynamic path imposed by their chemical composition, whilst solid state metallurgical transformations complete the final microstructure of the obtained solar-treated surface, as well as that of the heat-affected area, H.A.Z., (Figure 6d). In both material systems, the areas of dendritic growth (Figures 3 and 5)—at the bottom of the re-solidified pool, in contact to the nonmolten base metal—are indicative of the solidification starting points and the heat dissipation directions.
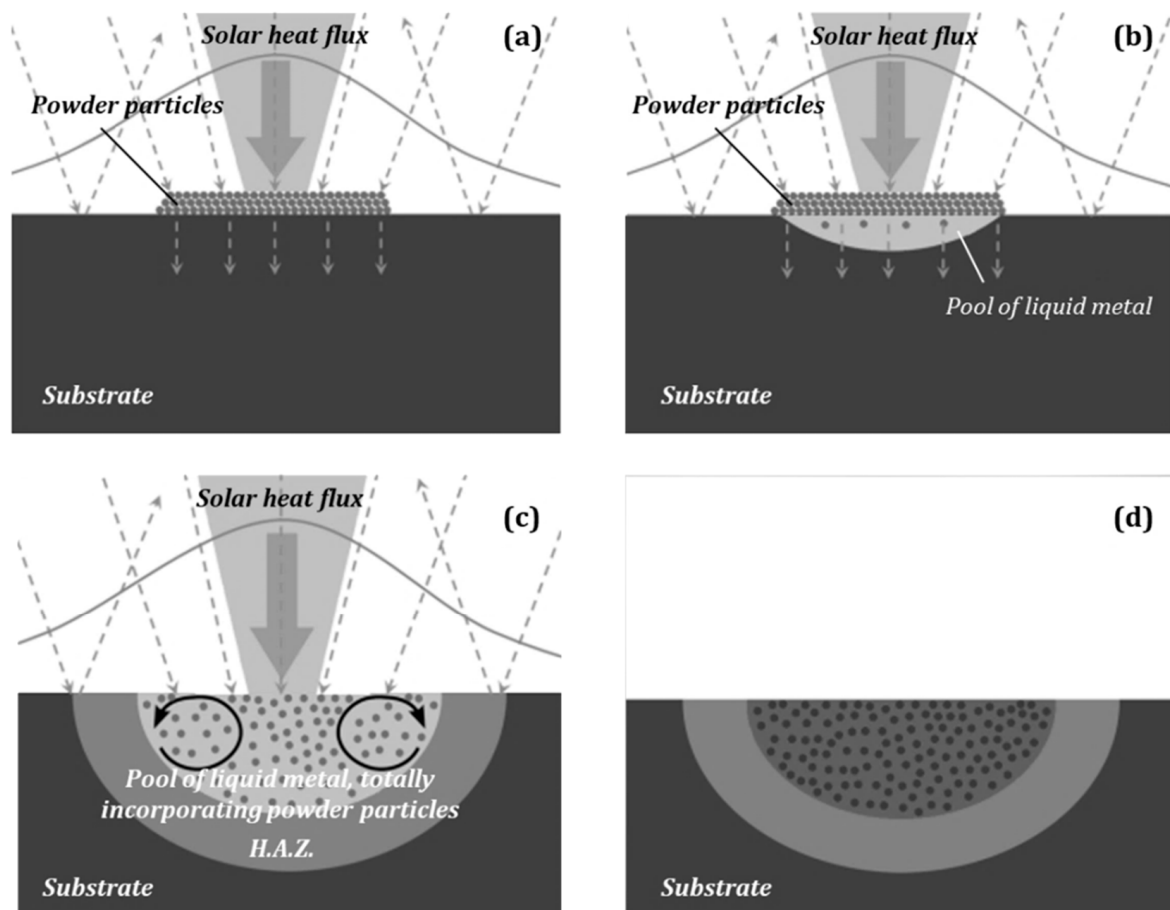

Figure 6. Simplified schematic representation of the successive stages that can be distinguished during surface solar processing: (**a**) absorption of concentrated solar energy by the area covered by the black-colored powder particles; (**b**) heat transfer to the metallic substrate and surface liquidation of the volume wherein temperature exceeded its characteristic melting value; (**c**) immersion and dispersion of the pre-deposited particles in the molten metallic pool; (**d**) re-solidified surface volume, consisting of dispersion (case of TiC powder) or total dilution (case of Cr_3C_2 powder) of the ceramic particles within the substrate metallic matrix and cooled to ambient temperature.

This physical model (Figure 6) is applied to describe thermal phenomena taking place during the particular solar processing. As depicted, the heat transfer associated with this process is time-dependent and rather complex, as it is governed by the:

- nature of coupling between the surface-heating source and the workpiece that consists of a powder layer onto a metallic substrate. This coupling is not purely diffusive, but in principle, is a combination of Beer—Lambert-type volumetric energy deposition and advection-diffusion of heat;
- thermal contact properties at the pre-deposited powder layer-metallic substrate interface,
- complexity of the metallurgical transformations taking place between the powder layer and substrate materials;
- changes in volume and shape of the molten region that are produced by the dispersion of the powder particles in the solar-affected region of the substrate materials.

It should be noted that the schematic description presented in Figure 6 does not include the process phases of dilatation of the metallic substrate during liquidation of the metal and shrinkage of the composite volume, which is the sum of layer and substrate material volumes during re-solidification and cooling to ambient temperature.

4. Inverse Thermal Analysis

The posing of the associated inverse thermal analysis problem can be derived from the above experimental observations, the surface temperature measurements and the generic physical model described. Given the known qualitative characteristics of the solar-heating process, thermal properties of the constitute materials, shapes and geometries of the powder-layer-substrate system at onset of heating and the re-solidified region after termination of process, and estimates of surface temperature as a function of time, the first step is to construct a parametric model structured for input of this information for prediction of temperature histories within the volume of processed workpieces. Then, the inverse problem is solved accordingly, constrained by the resulting molten volume of mixed material at the surface and estimated surface-temperature history, for the purpose of controlling treatment depth as a function of irradiation time. In principle, treatment depth would be defined by metallurgical transformations taking place within the volume of mixed material during processing. Temperature histories calculated by inverse thermal analysis would be used as input to transformation models and associated software for prediction of metallurgical transformations [26]. The inverse problem, as defined by the solar-heating process, consists of two separate parts, namely estimation of time-dependent temperature fields during heating and cooling, each one associated with the respective stage of the process. As revealed in what follows, more detailed information tends to be available for inverse thermal analysis during the cooling phase, owing to its accessibility by convenient measurement and post-process metallographic analysis.

Presented in this section is a parametric model for inverse thermal analysis of heat transfer through a thin layer of surface material, and a volume of an underlying substrate material, which is characteristic of the process considered here. This model, which uses the heat-kernel solution of the heat-conduction equation as ansatz [27], is given by:

$$T(x, t) = C(t)G(x, x_k, t) \tag{1}$$

and

$$T(x = x_k, t) = T_{Surface}(t) \tag{2}$$

for $t < t_h$, the heating period, and for $t > t_h$, the cooling period,

$$T(x, t) = C(t_h)G(x, x_k, t) \tag{3}$$

where:

$$G(x, x_k, t) = \frac{1}{\sqrt{4\pi\kappa_u t}}\exp\left[-\frac{(x - x_k)^2}{4\kappa_u t}\right] + \frac{W_0}{\sqrt{4\pi\kappa_u t}}\exp\left[-\frac{(x_{imag})^2}{4\kappa_u t}\right] \tag{4}$$

for $x \geq x_l$:

$$G(x, x_k, t) = \frac{W_1}{\sqrt{\pi\kappa_d t}}\exp\left[-\frac{1}{4t}\left(\frac{x - x_l}{\sqrt{\kappa_d}} + \frac{x_l - x_k}{\sqrt{\kappa_u}}\right)^2\right] \tag{5}$$

and for $x \geq x_s$:

$$G(x, x_k, t) = \frac{W_1}{\sqrt{\pi\kappa_d t}}\exp\left[-\frac{1}{4t}\left(\frac{x - x_s}{\sqrt{\kappa_s}} + \frac{x_s - x_l}{\sqrt{\kappa_d}} + \frac{x_l - x_k}{\sqrt{\kappa_u}}\right)^2\right] \tag{6}$$

where the weight coefficients W_0 and W_1 are given by:

$$W_0 = \frac{k_u\sqrt{\kappa_d} - k_d\sqrt{\kappa_u}}{k_u\sqrt{\kappa_d} + k_d\sqrt{\kappa_u}} \tag{7}$$

and

$$W_1 = \frac{2k_u\kappa_d}{\sqrt{\kappa_u}\left(k_u\sqrt{\kappa_d} + k_d\sqrt{\kappa_u}\right)} \tag{8}$$

The distance within the layered material from the surface (at x_k) is $(x - x_k)$, and the location of the interface between the thin-layer and the substrate is $(x_s - x_k)$. The quantities k_u, k_u are the estimated thermal conductivity and diffusivity of the thin-layer, and ks is the thermal diffusivity of substrate materials, respectively. The quantities x_l, k_d and k_d are adjustable phenomenological parameters for modeling thermal coupling of layer to substrate at their interface. Accordingly, the distance parameter x_l is not associated with an actual physical location within the layer system. For $x < x_1$, $x_{imag} = x + x_k - 2x_l$, which is also a phenomenological parameter, is not associated with the image-distance of a physical location. Similarly, although k_d and k_d are formally conductivity and diffusivity, respectively, they do not represent bulk material properties, relevant schema is presented in Figure 7. The function *C(t)* is specified by the boundary and initial conditions defined by Equations (2) and (3), respectively. Specifically, the model assigns two conditions during heating, namely the measured surface temperature and the time period of heating, and one after termination of heating, the time period of cooling. Equations (4)–(8) are the heat-kernel solution to the heat-conduction equation for a one-dimensional system consisting of a layer of a material of finite thickness, on a substrate of essentially infinite extent, where the layer and substrate materials have different thermal properties [25], and there exists complex coupling between the surface-heating source and workpiece, that can be a combination of:

- Beer—Lambert-type volumetric energy-deposition and advection diffusion of heat;
- differentiation of the thermal properties of the surface layer-substrate at the contact interface;
- nonuniform mixing of layer and substrate materials;
- temporal changes of the volume and the exact shape of the molten pool.

This complex coupling is modeled via the adjustable phenomenological parameters x_l, k_d and κ_d; whilst for the TiC/steel system, the estimated thermal properties and model parameters are: k_u = 5.64 W/(kg °C), κ_u= 1.306 × 10^{-6} m^2/s [30], κ_s = 1.483 × 10^{-5} m^2/s and x_s = 1.5 mm, and those for the Cr$_3$C$_2$/ steel system are: k_u = 15 W/(kg °C), κ_u= 1.612 × 10^{-5} m^2/s [31–34], κ_s = 1.483 × 10^{-5} m^2/s and x_s = 3.0 mm. For the analyses whose results are shown in Figures 8–13, the quantity g is an adjustable coefficient for assigning values to the phenomenological parameters k$_d$ and *kd*, which is completed by scaling of measured thermal properties of material layers.

The results of inverse thermal analyses for the solar processing of the TiC/common steel system are presented in Figures 8–10, whilst those of the Cr_3C_2/common steel system are presented in Figures 11–13. In all cases, the values of the adjustable phenomenological parameters x_l, k_d and κ_d are provided in the figure captions.

Shown in Figure 8 are different volumetric temperature distributions at completion of surface heating of the TiC/common steel system, which is on a timescale that is small relative to that of heat conduction in the layered material (see inset of Figure 9b). As indicated in Figure 8, the shapes of these temperature distributions are a function of the phenomenological parameters x_l, k_d and k_d. Referring to Figure 8, the temperature distributions for $x_l = (70/100)1.5$ mm and $x_l = (10/100)1.5$ mm correspond, respectively, to total and partial volumetric energy deposition.
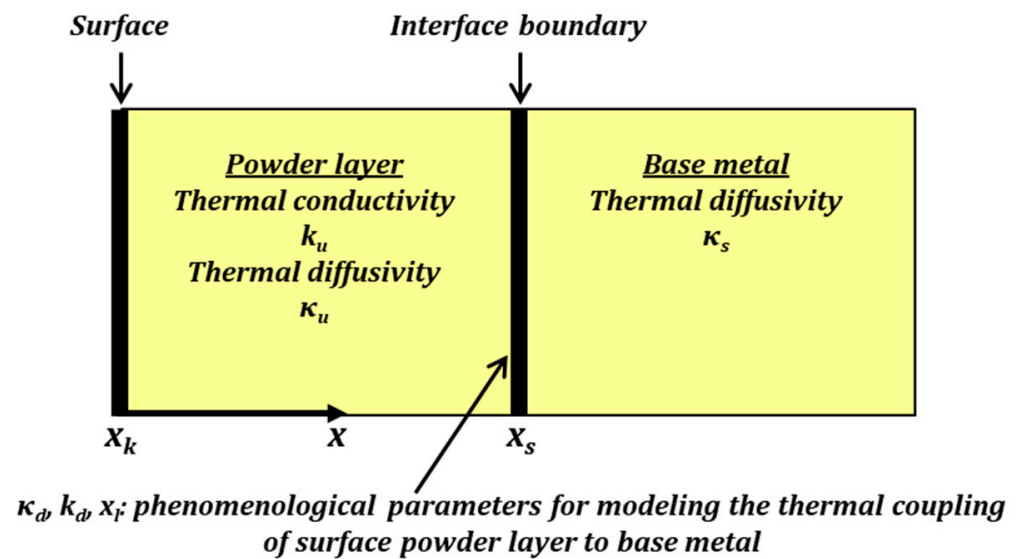

Figure 7. 2D-Schematic representation of regions of the layered-system, and associated material properties and phenomenological parameters for the 1D model defined by Equations (1)–(7).
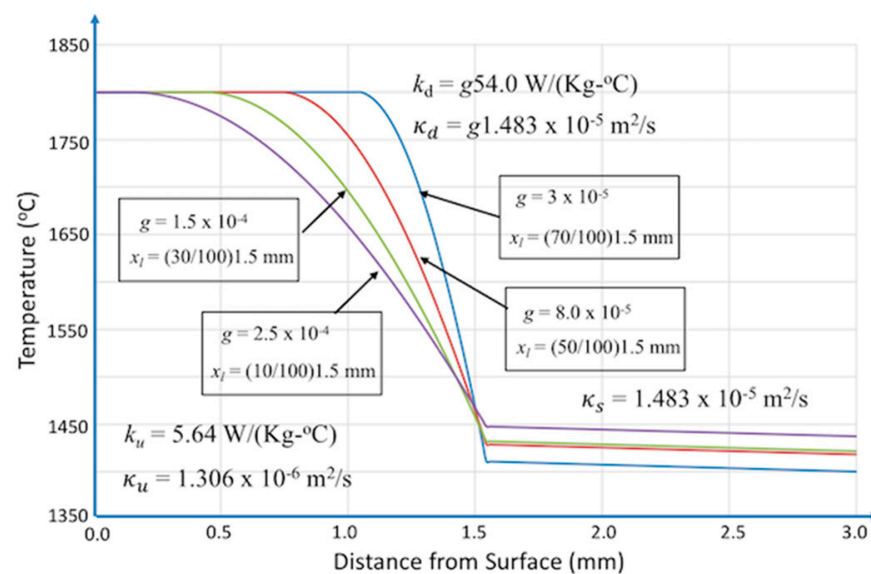

Figure 8. Temperature field at end of heating period as a function of adjustable phenomenological parameters x_l, k_d and κ_d (system TiC/common steel).
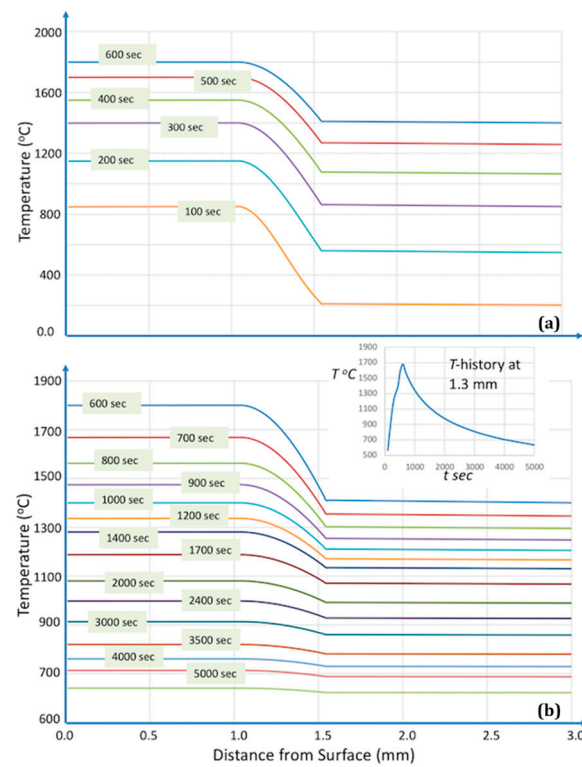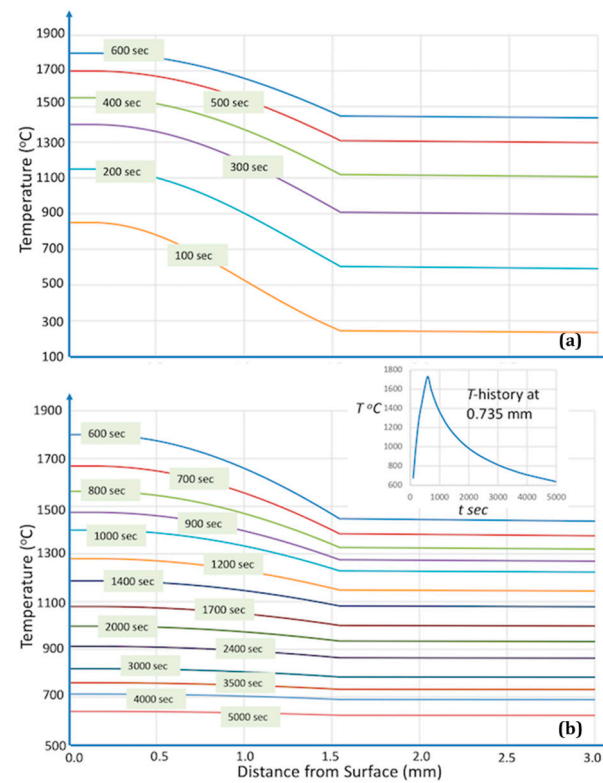
Figure 9. Simulations for the system TiC/common steel at $x_l = (70/100)$ 1.5 mm: (**a**) heating period; (**b**) cooling period [$k_d = g54.0$ W/(kg. °C), $\kappa_d = g1.483 \times 10^{-5}$ m^2/s, where $g = 3 \times 10^{-5}$].

Figure 10. Simulations for the system TiC/common steel at $x_l = (10/100)$ 1.5 mm: (**a**) heating period; (**b**) cooling period [$k_d = g54.0$ W/(kg. °C), $\kappa_d = g1.483 \times 10^{-5}$ m^2/s, where $g = 2.5 \times 10^{-4}$].
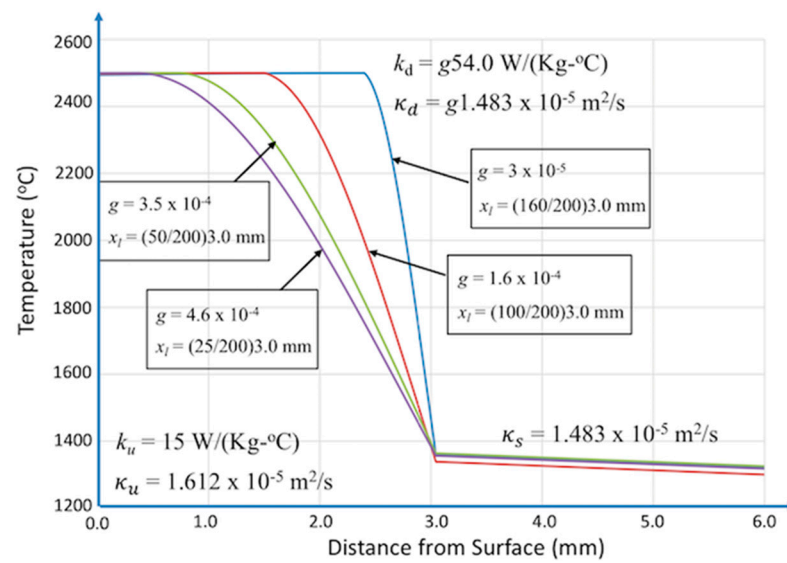
Figure 11. Temperature field at end of heating period as a function of adjustable phenomenological parameters x_l, k_d and κ_d (system Cr_3C_2/common steel).
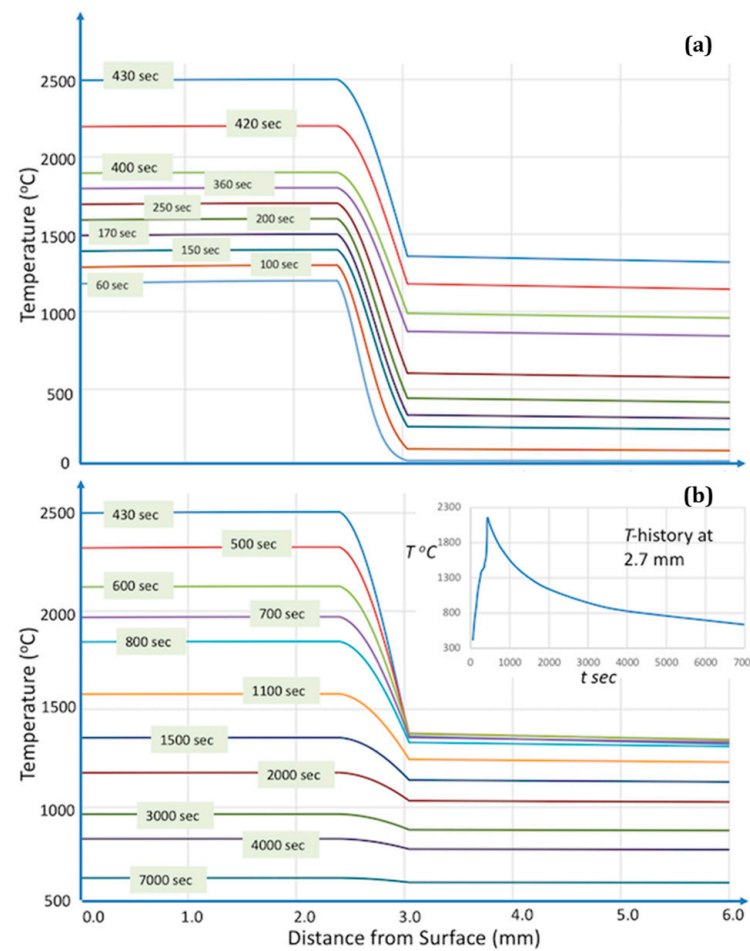

Figure 12. Simulations for the system Cr_3C_2/common steel at $x_l = (160/200)$ 3.0 mm: (**a**) heating period; (**b**) cooling period [$k_d = g54.0$ W/(kg$-$°C), $\kappa_d = g1.483 \times 10^{-5}$ m²/s, where $g = 3 \times 10^{-5}$].
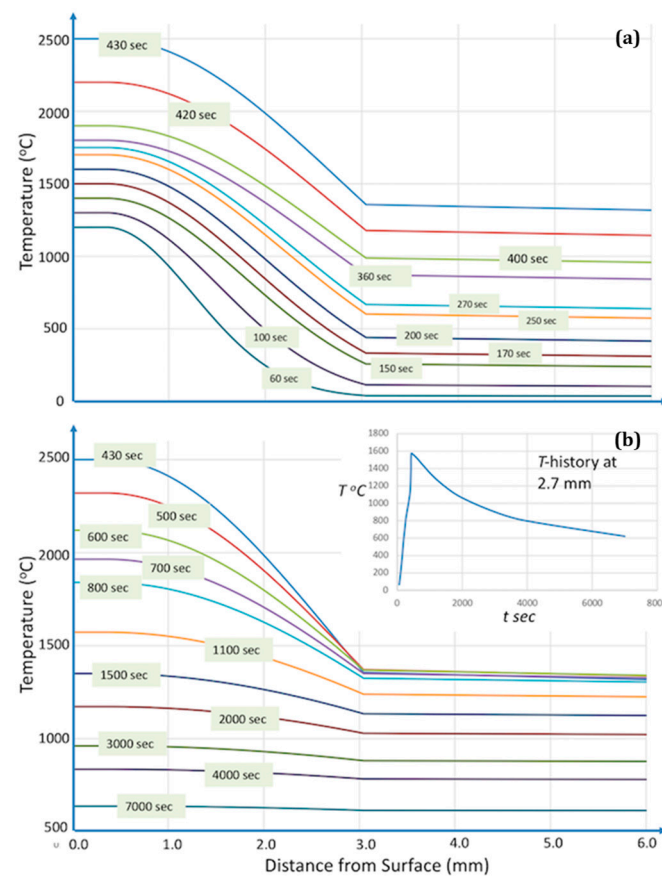
Figure 13. Simulations for the system Cr_3C_2/common steel at $x_l = (25/200)3.0$ mm: (**a**) heating period; (**b**) cooling period [$k_d = g54.0$ W/(kg−°C), $\kappa_d = g4.6 \times 10^{-4}$ m^2/s, where $g = 3 \times 10^{-5}$].

Shown in Figures 9 and 10 are heating and cooling periods for the TiC/common steel system, corresponding, respectively, to total and partial energy deposition during surface heating. Comparison of temperature histories shown in Figures 9 and 10 indicates a relative insensitivity of temperature histories in terms of trend during cooling to the range of volumetric energy deposition from partial to total. This result is significant in that estimating the temperature distribution at completion of surface heating, because the complexity of the solar heating process, consisting of multiple coupled physical processes, poses a more difficult problem than estimating the temperature history in the layered system, which is based on heat conduction alone. In particular, of significance is that the temperature distribution at completion of surface heating provides a boundary condition, in terms of the heat conduction equation [27], for prediction of temperature histories in the layer system. There is a direct correlation between maximum temperature at layer-substrate interface and the extent of energy deposition at the surface (see insets of Figures 9 and 10).

From a practical point of view, the feasibility of a quantitative analysis of temperature fields developed during solar processing could be used as a useful tool for the prediction of the microstructure of the solar-treated surface layers (e.g., top layer reinforced by a dispersion of TiC particles, dendritic growth at the bottom melt pool area in contact with the unmolten metal), the extent and the microstructure of the underlying heat affected zone, as well as the solid state modifications of the base metal microstructure (e.g., stress relief, grains growth).

The analysis whose results are shown in Figures 11–13, for the Cr_3C_2/common steel system, follows the same procedure as above for the TiC/common steel system. Shown in Figure 11 are different volumetric temperature distributions at completion of surface heating of the Cr_3C_2/common steel system, ranging from partial to total volumetric energy deposition. Referring to Figure 11, the temperature distributions for $x_l = (160/200)$ 3.0 mm

and $x_l = (25/200)\ 3.0$ mm correspond, respectively, to total and partial volumetric energy deposition. Shown in Figures 12 and 13 are heating and cooling periods for the Cr_3C_2/common steel system, corresponding, respectively, to total and partial energy deposition during surface heating. As for the previous analysis, comparison of temperature histories shown in Figures 12 and 13 indicates a relative insensitivity of temperature histories with respect to trend during cooling to the range of volumetric energy deposition from partial to total, and direct correlation between maximum temperature at layer-substrate interface and the extent of energy deposition at the surface (see insets of Figures 12 and 13).

From a practical point of view, the verification of the quantitative description potency in the case of Cr_3C_2 powder that is totally dissolved in the liquid ferrous matrix constitutes strong evidence for the development of a generic model, valid for the quantitative description of solar surface processing of other pre-deposited carbide powder/base metal systems, whatever the metallurgical reactions could be. Thus, such an inverse thermal analysis could be applied as a prediction tool for optimising the solar processing parameters, in order to control the microstructure and, consequently, the mechanical properties and in-service performance of solar-treated material systems.

Overall, the energy deposition process is multiscale with respect to heat transfer, owing to a region of rapid heating (top, directly irradiated layer) being coupled to one of purely diffusive heat transfer (underlying workpiece volume), thus posing a specific problem for inverse thermal analysis, as discussed above (see Figures 6 and 7). The model, Equations (1)–(8), and simulations using this model, whose results are shown in Figures 8–13, examines the nature of the coupling between two regions where heat transfer occurs on different timescales, and is controlled by characteristics of their interface coupling. The timescale and rate for heat transfer at the top layer can be estimated by in-situ surface-temperature measurements and ex-situ optical microscopy observations of the volume of the workpiece, while rate for heat transfer within the workpiece is predictable given the thermal diffusivity and observed microstructural changes within the workpiece, see Figures 2–5. The unknown characteristic of the layered system, to be estimated by inverse thermal analysis, is the coupling between these regions.

What is known a priori concerning the thermal physics of interfaces between two materials having different thermal properties is represented formally by the model Equations (1)–(8). Considered in this model is that even for the ideal case, where thermal contact resistance is not present, differences in thermal diffusivity are sufficient to induce reflected thermal transport during time-dependent heat transfer across an interface [27]. For the nonideal case, which should be assumed for the process considered here, contact resistance at the interface will contribute to reflected heat transfer within the top layer. The characteristics of contact resistance with respect to reflected heat transfer is by nature extremely complex, having multivariable dependence, and thus modelled using phenomenological parameters. The results of simulations show that a range of reasonable estimated interface-coupling strengths, defined by phenomenological adjustable parameters (see Figures 8 and 11), can be determined by inverse thermal analysis, given the measured boundary constraints imposed by the top-layer and workpiece regions. With respect to process control, these simulations show that characteristics of the interface coupling are a significant controlling factor for heat transfer, as demonstrated by comparison of Figures 9 and 12 to Figures 10 and 13, respectively, and thus may suggest methods of process control in the future. Overall, the solar heating process is defined by rate of solar-energy coupling to the top layer, and subsequently, coupling of this energy to the workpiece, which is a function of interface heat-transport characteristics.

Recently, such an inverse analysis approach has been successfully adopted for the evaluation of the solidification path of stainless steel melts [35] and microstructure modifications of Inconel 718 [36], both taking place during additive manufacturing via Selective Laser Melting.

5. Conclusions

The purpose of this study was to describe a generic parametric model for the estimation of temperature histories within bi-material workpieces subjected to surface treatment applying Concentrated Solar Energy. During solar processing, details on the exact amount of the volumetric energy deposition within the workpiece are difficult to be determined. Thus, reverse thermal analysis constitutes a powerful tool for describing quantitatively the temporal and spatial temperature evolution, based on post-processing metallographic observations of the microstructures obtained.

In summary, the CSE surface treatment of two carbide powder/common steel systems resulted in reinforced surface clads that have been previously proven to exhibit acceptable machinability using conventional cutting tools and superior in-service wear resistance. The present first attempt revealed the potential of applying reverse thermal analysis and parametric modeling for the prediction of the temperature history within the CSE-affected area and to correlate, by extension, the solar-layers performance to the solar processing parameters.

References

1. Pitts, J.R.; Tracy, E.; Shinton, Y.; Fields, C.L. Applications of solar energy to surface modification processes. *Crit. Rev. Surf. Chem.* **1993**, *2*, 247–269.
2. Rodríguez, G.P.; de Damborenea, J.J.; Vázquez, A.J. Surface hardening of steel in a solar furnace. *Surf. Coat. Technol.* **1997**, *92*, 165–170. [CrossRef]
3. Flamant, G.; Ferriere, A.; Laplaze, D.; Monty, C. Solar processing of materials: Opportunities and new frontiers. *Sol. Energy* **1999**, *66*, 117–132. [CrossRef]
4. Rodríguez, G.P.; Herranz, G.; Romero, A. Solar gas nitriding of Ti6Al4V alloy. *Appl. Surf. Sci.* **2013**, *283*, 445–452. [CrossRef]
5. Pantelis, D.I.; Psyllaki, P.; Sarafoglou, C. Surface alloying on cast iron using concentrated solar energy. *Fonderie Fondeur Aujourd'hui* **2002**, *211*, 23–33.
6. Mourlas, A.; Psyllaki, P.; Pantelis, D. Anti-wear TiC-based surface layers using concentrated solar energy. *Key Eng. Mater.* **2016**, *674*, 296–301. [CrossRef]
7. Mourlas, A.; Pavlidou, E.; Vourlias, G.; Rodríguez, J.; Psyllaki, P. Concentrated solar energy for in-situ elaboration of wear-resistant composite layers. Part I: TiC and chromium carbide surface enrichment of common steels. *Surf. Coat. Technol.* **2019**, *377*, 124882. [CrossRef]
8. Mourlas, A.; Pavlidou, E.; Vourlias, G.; Rodríguez, J.; Psyllaki, P. Concentrated solar energy for in-situ elaboration of wear-resistant composite layers. Part II: Tungsten carbide surface enrichment of common steels. *Surf. Coat. Technol.* **2019**, *375*, 739–751. [CrossRef]
9. Pantelis, D.I.; Griniari, A.; Sarafoglou, C. Surface alloying of pre-deposited molybdenum-based powder on 304L stainless steel using concentrated solar energy. *Sol. Energy Mat. Sol. Cells* **2005**, *89*, 1–11. [CrossRef]
10. Fernández-González, D.; Ruiz-Bustinza, Í.; González-Gasca, C.; Piñuela-Noval, J.; Mochón-Castaños, J.; Sancho-Gorostiaga, J.; Verdeja, L.F. Concerntrated solar energy applications in materials science and metallurgy. *Sol. Energy* **2018**, *170*, 520–540. [CrossRef]
11. International Energy Agency. Renewable Energy for Industry: From Green Energy to Green Materials and Fuels. 2017. Available online: https://www.iea.org/publications/freepublications/publication/ (accessed on 25 March 2023).

12. Sánchez Bautista, C.; Rodríguez, G.P.; Ferriere, A. Numerical modelling of the solar cladding process. *Surf. Coat. Technol.* **2008**, *202*, 1594–1605. [CrossRef]
13. Li, B.; Oliveira, F.A.C.; Rodríguez, J.; Fernandes, J.C.; Rosa, L.G. Numerical and experimental study on improving temperature uniformity of solar furnaces for materials processing. *Sol. Energy* **2015**, *115*, 95–108. [CrossRef]
14. Romero, A.; García, I.; Arenas, M.A.; López, V.; Vázquez, A. High melting point materials welding by concentrated solar energy. *Sol. Energy* **2013**, *95*, 131–143. [CrossRef]
15. Román, R.; Cañadas, I.; Rodríguez, J.; Hernández, M.T.; González, M. Solar sintering of alumina ceramics: Microstructural development. *Sol. Energy* **2008**, *82*, 893–902. [CrossRef]
16. Gutiérrez-López, J.; Levenfeld, B.; Várez, A.; Pastor, J.Y.; Cañadas, I.; Rodríguez, J. Study of the densification, mechanical and magnetic properties of Ni-Zn ferrites sintered in a solar furnace. *Ceram. Int.* **2015**, *41*, 6534–6541. [CrossRef]
17. Herranz, G.; Romero, A.; DeCastro, V.; Rodríguez, G.P. Processing of AISI M2 high speed steel Reinforced with vanadium carbide by solar sintering. *Mater. Des.* **2014**, *54*, 934–946. [CrossRef]
18. Cambronero, L.E.G.; Cañadas, I.; Martínez, D.; Ruiz-Román, J.M. Foaming of aluminium-silicon alloy using concentrated solar energy. *Sol. Energy* **2010**, *84*, 879–889. [CrossRef]
19. Ozisik, M.N.; Orlande, H.R.B. *Inverse Heat Transfer, Fundamentals and Applications*; Taylor & Francis: New York, NY, USA, 2000.
20. Kurpisz, K.; Nowak, A.J. *Inverse Thermal Problems—Computational Engineering*; WIT Press: Boston, MA, USA, 1995.
21. Alifanov, O.M. *Inverse Heat Transfer Problems*; Springer: Berlin/Heidelberg, Germany, 1994.
22. Beck, J.V.; Blackwell, B.; St. Clair, C.R., Jr. *Inverse Heat Conduction: Ill-Posed Problems*; John Wiley & Sons Inc.: New York, NY, USA, 1985.
23. Beck, J.V. Inverse Problems in Heat Transfer with Application to Solidification and Welding. In Proceedings of the 5th Conference on Modeling of Casting, Welding and Advanced Solidification Processes, Davos, Switzerland, 16–21 September 1990.
24. Beck, J.V. Inverse Problems in Heat Transfer. In *Mathematics of Heat Transfer*; Tupholme, G.E., Wood, A.S., Eds.; Oxford University Press: New York, NY, USA, 1998; pp. 13–24.
25. Lambrakos, S.G. Parametric Modeling of welding processes using numerical-analytical basis functions and equivalent source distributions. *J. Mater. Eng. Perform.* **2016**, *25*, 1360–1375. [CrossRef]
26. Prosgolitis, C.G.; Lambrakos, S.G.; Zervaki, A. Phase-Field Modeling of Nugget Zone for a AZ31-Mg-Alloy Friction Stir Weld. *J. Mater. Eng. Perform.* **2018**, *27*, 5102–5113. [CrossRef]
27. Carslaw, H.S.; Jaegar, J.C. *Conduction of Heat in Solids*, 2nd ed.; Oxford University Press: New York, NY, USA, 1986; p. 374.
28. Zervaki, A.D.; Mourlas, A.G.; Psyllaki, P.P.; Lambrakos, S.G. Parametric Model of Concentrated Solar Energy Surface Processing. In Proceedings of the Advances in Welding & Additive Manufacturing Research Conference 2022, Miami, FL, USA, 13–16 June 2022.
29. Rodríguez, J.; Cañadas, I.; Zarza, E. New PSA high concentration solar furnace SF40. *AIP Conf. Proc.* **2016**, *1734*, 070028.
30. Shackelford, J.F.; Han, Y.-H.; Kim, S.; Kwon, S.-H. *CRC Materials Science and Engineering Handbook*, 4th ed.; Taylor & Francis: Boca Raton, FL, USA, 2015; pp. 50, 263, 279.
31. Pankratz, L.B. *Thermodynamic Properties of Carbides, Nitrides, and Other Selected Substances*; US Department of the Interior, Bureau of Mines: Washington, DC, USA, 1994; 696, p. 223.
32. Desorbo, W. Heat Capacity of Chromium Carbide (Cr_3C_2) from 13 to 300 °K. *J. Am. Chem. Soc.* **1953**, *75*, 1825–1827. [CrossRef]
33. Oriani, R.A.; Murphy, W.K. The Heat Capacity of Chromium Carbide (Cr_3C_2). *J. Am. Chem. Soc.* **1954**, *76*, 343–345. [CrossRef]
34. Kelley, K.K.; Boericke, F.S.; Moore, G.E.; Huffman, E.H.; Bangert, W.M. *Thermodynamic Properties of the Carbides of Chromium*; US Department of the Interior, Bureau of Mines: Washington, DC, USA, 1944; 662, pp. 7–15.
35. Abolhasani, D.; Hossein Seyedkashi, S.M.; Kang, N.; Kim, Y.J.; Woo, Y.Y.; Moon, Y.H. Analysis of Melt-Pool Behaviors during Selective Laser Melting of AISI 304 Stainless-Steel Composites. *Metals* **2019**, *9*, 876. [CrossRef]
36. Tabaie, S.; Rézaï-Aria, F.; Jahazi, M. Microstructure Evolution of Selective Laser Melted Inconel 718: Influence of High Heating Rates. *Metals* **2020**, *10*, 587. [CrossRef]